

Ultra-low loss and large bandwidth fiber-to-chip edge coupler for aluminum oxide photonic platform at UV-visible wavelengths

Chupao Lin, Max Kiewiet, Robin R. Petit, Jolien Dendooven, Nicolas Le Thomas, Christophe Detavernier and Bart Kuyken

Abstract—Achieving low-loss coupling between single-mode fibers and photonic integrated circuits plays a crucial role in emerging enabling technologies including quantum information, advanced imaging, and precision metrology. High coupling efficiency in the UV/visible spectrum remains challenging due to the small waveguide dimensions at shorter wavelengths. Here, we present an ultra-low loss edge coupler made of a $\text{SiO}_x/\text{AlO}_x$ mode converter. The coupling loss between a standard single-mode fiber and an AlO_x waveguide below 0.31 dB and 0.62 dB is experimentally demonstrated at a working wavelength of 375 nm and 405 nm, respectively. The design exhibits a large bandwidth of 110 nm below 2.6-dB loss over the entire operating wavelength range of the single mode fiber, as obtained from the simulation. This coupler not only facilitates low-loss fiber-to-chip coupling but also significantly reduces spurious light scattering, making it particularly valuable for applications in PIC-based far-field advanced microscopy and trapped-ion quantum information systems.

Index Terms—Edge coupler, photonic integrated circuits, spot size converter, aluminum oxide, UV, visible

I. INTRODUCTION

ULTRAVIOLET (UV) and visible light are critical for enabling light-matter interaction for applications such as quantum information processing [1], precision metrology [2], and life sciences [3]. Traditional photonic platforms based on silicon nitride (SiN_x) and silicon are well-established but suffer from high material absorption in the short visible and UV spectral ranges, limiting their applicability. Recent advances in photonic integrated circuits (PICs) using amorphous and polycrystalline AlO_x address this gap, as AlO_x offers a broad transparency spectrum extending from the UV to infrared wavelengths and is compatible with complementary metal-oxide-semiconductor (CMOS) fabrication processes [4]–[6]. While PICs have been extensively utilized for telecom and datacom applications in the near-infrared [7]–[10], their development at UV and short visible wavelengths is still in its early stages. Beyond the advantages of low cost and scalability for mass production, PICs surpass bulk optics in robustness

This work is partially supported by the Horizon Europe project Qu-PIC (Grant Agreement No.101135845).

Chupao Lin, Max Kiewiet, Nicolas Le Thomas and Bart Kuyken are with the Photonics Research Group, INTEC Department, Ghent University-imec, 9052 Ghent, Belgium, and also with the Center for Nano- and Biophotonics, Ghent University, 9052 Ghent, Belgium (e-mail: chupao.lin@ugent.be), Robin Petit, Jolien Dendooven and Christophe Detavernier are with the CoCooN group, Department of Solid State Sciences, Ghent University, 9000 Ghent, Belgium. (Corresponding author: Chupao Lin)

Manuscript received December 19, 2024; revised February 16, 2025.

and compactness, making them highly attractive for emerging applications. AlO_x -based PICs, in particular, show promise for diverse fields, including UV far-field autofluorescence structured illumination microscopy [5], [11], quantitative phase imaging [12], and trapped ion addressing [13], [14]. These advancements highlight the transformative potential of AlO_x PICs for UV-visible applications, enabling new possibilities in precision optical systems.

The typical methods for fiber-to-chip coupling in photonic platforms are grating couplers and edge couplers. However, achieving high coupling efficiency via a grating coupler on an AlO_x photonic platform presents significant challenges. One primary issue is the relatively low refractive index contrast between AlO_x and SiO_2 cladding (0.21–0.32), which limits the coupling efficiency of grating couplers to approximately 10%. Additionally, controlling the SiO_2 film thickness with high precision is crucial at shorter wavelengths to enhance coupling efficiency by leveraging back reflection from the silicon substrate, making this method technically demanding. Silicon exhibits a high absolute refractive index (e.g., $n=6.84$ at $\lambda=375$ nm) at UV-visible wavelengths. This results in substantial light reflection at the SiO_2/Si interface, which interferes with light coupled into the grating. To achieve constructive interference and maximize coupling efficiency, the thickness of the buried oxide needs to be controlled with a precision of ≤ 50 nm. Due to these limitations, most fiber-to- AlO_x integrated waveguide coupling at UV-visible wavelengths is currently achieved using edge coupling. Due to the significant mode mismatch, the coupling loss between the single-mode fiber and the AlO_x waveguide is high, reaching approximately 8 dB at $\lambda=375$ nm. To enhance coupling efficiency, advanced taper designs such as adiabatic tapers and double-tip tapers have been proposed. These designs have demonstrated improved performance, achieving coupling losses of 6.7 dB [15] and approximately 3 dB at $\lambda=405$ nm [16], respectively. Edge coupling remains the preferred approach for UV-visible wavelengths, offering a more practical solution for high-efficiency fiber-to-chip coupling in AlO_x -based photonic platforms.

In this work, we demonstrated an ultra-low loss and broadband edge coupler based on a $\text{SiO}_x/\text{AlO}_x$ mode converter. The edge coupler is optimized for maximizing the coupling efficiency between a single AlO_x waveguide and a standard single-mode fiber (SM300, Thorlabs). A coupling loss of 0.31 dB and 0.18 dB is achieved at a wavelength of 375 nm

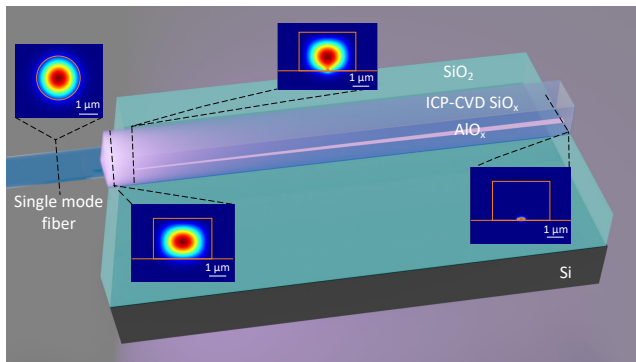


Fig. 1: Illustration of the edge coupler made of SiO_x and AlO_x . The insets show the evolution of the modal profiles along the length of the edge coupler.

for transverse electric (TE) and transverse magnetic (TM) polarizations, respectively. At a wavelength of 405 nm, the values are 0.29 dB and 0.62 dB, respectively. These findings align with the simulation outcomes. Additionally, the edge coupler has a coupling loss below 2.6 dB across the entire operating wavelength range of a single-mode fiber, spanning from 320 nm to 430 nm. It is anticipated to serve as a pivotal component in the development of low-loss fiber-to-chip coupling in the UV and short visible range for AlO_x photonic integrated platforms.

II. PRINCIPLE AND SIMULATION

The schematic of the edge coupler is depicted in Fig. 1. The light is coupled from the SM fiber, which is commercially available from Thorlabs and has a working wavelength ranging from 320 to 430 nm, to a SiO_x waveguide. The SiO_x is deposited by inductive plasma enhanced-chemical vapor deposition (ICP-CVD). The refractive index of the SiO_x (1.480) is slightly higher than that of SiO_2 thermally oxidized on a silicon wafer (1.476), enabling the formation of a weakly confined optical mode in the ICP-CVD SiO_x , as shown in Fig. 2(a). Subsequently, light is transferred from the ICP-CVD SiO_x waveguide to a single mode AlO_x waveguide through an AlO_x adiabatic taper functioning as a mode converter. The SiO_x layer also serves as the top cladding for AlO_x waveguides. This edge coupler efficiently transitions light from the optical mode of $\sim 2.3 \times 2.3 \mu\text{m}$ in an SM fiber to a confined mode of $0.45 \times 0.12 \mu\text{m}$ in AlO_x waveguide. The evolution of the mode profiles across the fiber, ICP-CVD SiO_x waveguide, adiabatic taper, and AlO_x waveguide is illustrated in the insets of Fig. 1.

Mode overlapping between the optical fiber and the SiO_x waveguide is one of the critical parameters for achieving high coupling efficiency and minimizing spurious light scattering from the input. Greater mode overlap results in more light being coupled into the SiO_x waveguide, thereby reducing light scattered into free space. In certain applications such as PIC-based advanced microscopy [11] and PIC-based trapped ion quantum information [13], scattered light can significantly contribute to background noise, especially when the area

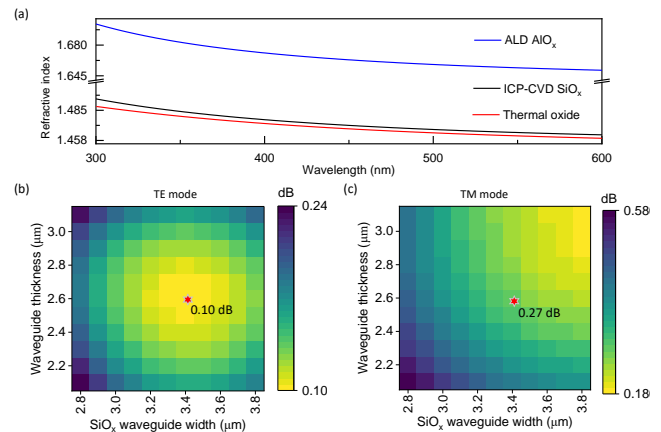


Fig. 2: (a) Optical dispersion curves of ALD- AlO_x , ICP-CVD SiO_x , and thermally oxidized SiO_2 . (b-c) Coupling loss maps between a single mode fiber and SiO_x waveguide for TE-polarized and TM-polarized light, respectively.

of interest is positioned a few to hundreds of micrometers above the chip plane. In this work, a MODE solver (Ansys Lumerical) is employed to analyze the coupling loss due to mode mismatch. The refractive index of the fiber core and cladding, provided by the supplier, are 1.4731 and 1.4673, respectively, at a working wavelength of 375 nm. The fiber core diameter is approximately $2.3 \mu\text{m}$. To optimize coupling efficiency, the width and height of the SiO_x waveguide are systematically varied in 100 nm steps, ranging from 2.8 to 3.8 μm for the width and from 2.1 to 3.1 μm for the height. Due to the circularly antisymmetric geometry of the SiO_x waveguide, the coupling loss is polarization-dependent, as shown in Fig. 2(b) and (c). Since TE polarization light is more commonly used in photonic integrated circuits, the waveguide dimensions are optimized to minimize the coupling loss for TE polarization in this work. The lowest coupling loss of 0.1 dB for TE-polarized light is achieved with a waveguide dimension of $3.4 \mu\text{m} \times 2.6 \mu\text{m}$, while the coupling loss for TM-polarized light under the same conditions is 0.27 dB.

Coupling light from the SiO_x waveguide to the AlO_x waveguide is facilitated by an AlO_x taper, simulated using an eigenmode expansion (EME) solver (Ansys Lumerical). Figure 3(a) illustrates the relationship between the taper length and the coupling loss from the fiber to the AlO_x waveguide. The taper width transitions linearly from 50 nm to 450 nm, matching the width of the AlO_x waveguide. The coupling loss converged at a taper length of 350 μm , reaching a minimum value of 0.15 dB for TE-polarized light and 0.28 dB for TM-polarized light. The edge coupler demonstrates high tolerance to fiber displacement for both TE and TM modes, as shown in Fig. 3(b) and 3(c). The dashed circular lines indicate that the coupler maintains a low loss of 1 dB and 3 dB for fiber displacements of $\pm 500 \text{ nm}$ and $\pm 1 \mu\text{m}$, respectively. Additionally, the coupler exhibits high tolerance to tip width variation caused by fabrication errors, as depicted in Fig. 3(d). Due to processing discrepancies between the designed and fabricated feature sizes, robustness to dimensional variations

is critical. The coupler maintains a low insertion loss below 1 dB for both TE and TM polarizations when the tip width varies between 10 nm and 90 nm.

The optical dispersion characteristics of the guided modes in the SiO_x waveguide were analyzed using a MODE solver, revealing its operational bandwidth (Fig. 3(e)). The waveguide supports guided modes within a wavelength range of 250 nm to 500 nm, as the mode remains confined when the effective index exceeds that of the cladding. The simulation results for the device's bandwidth are compared with experimental data in the Measurement Section.

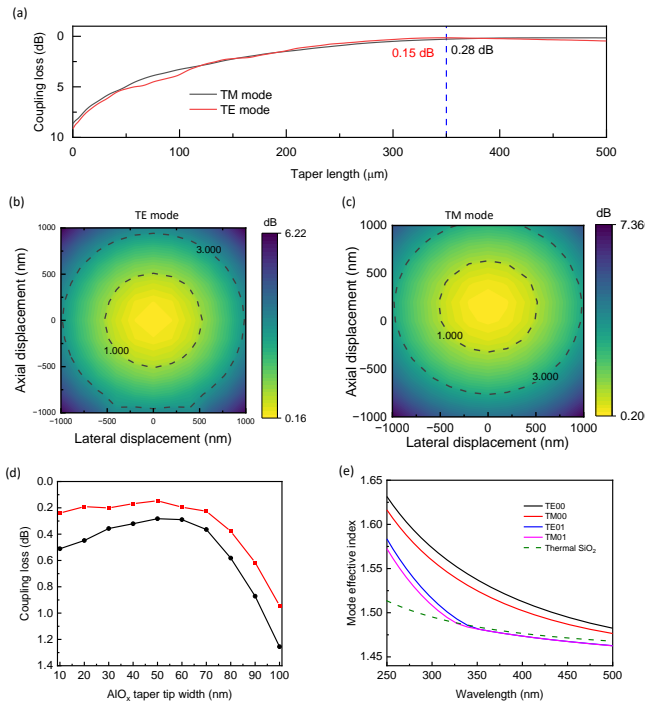


Fig. 3: (a) Relationship between the coupling loss of the edge coupler and the AlO_x taper length. The red and black lines represent the cases for TE and TM modes, respectively. (b-c) Maps of coupling loss as a function of the lateral and axial displacement of the optical fiber for TE and TM modes, respectively. (d) Relationship between coupling loss and the tip width of the AlO_x taper for TE (red line) and TM (black line) modes, respectively. (e) Optical dispersion of guided modes in AlO_x waveguides and thermally oxidized SiO_2 .

III. FABRICATION

The fabrication of the edge coupler is illustrated in Figure 4, consisting of two primary steps to sequentially pattern AlO_x and SiO_x waveguides. The process begins with a bare silicon wafer onto which a 120 nm-thick AlO_x thin film is deposited using ALD technique using the trimethylaluminum (TMA) and H_2O precursors at 300 $^\circ\text{C}$. Subsequently, A layer of SiN_x is deposited on top of the AlO_x via plasma-enhanced chemical vapor deposition (PECVD) at 270 $^\circ\text{C}$, serving as a hard mask for the AlO_x etching step. To pattern the SiN_x layer, an e-beam resist (ARP 6200.09) is spin-coated onto the chip and exposed using e-beam lithography (Raith Voyager). After the

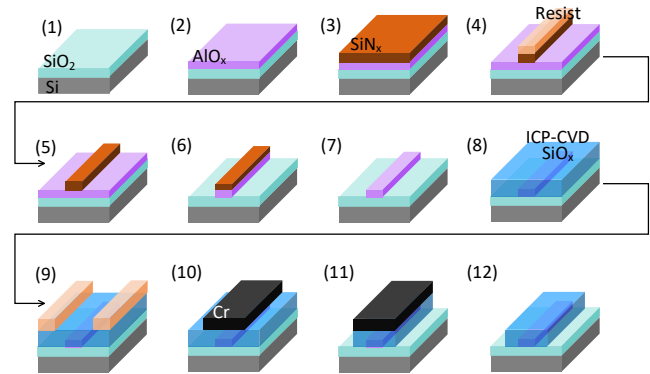


Fig. 4: Process flow of the edge coupler fabrication for the AlO_x photonic platform.

resist development, the SiN_x layer is etched in reactive ion etcher (RIE) using a fluorine-based gas mixture ($\text{CF}_4/\text{SF}_6/\text{H}_2$). The pattern of SiN_x is then transferred to the underlying AlO_x layer via inductively coupled plasma-reactive ion etching (ICP-RIE) with a chlorine-based etching gas mixture ($\text{BCl}_3/\text{Cl}_2/\text{Ar}$). Once the SiN_x hard mask is removed to avoid strong material absorption at UV and visible wavelength range, the fabrication of the AlO_x waveguide is completed. The fabrication of SiO_x waveguide begins with the deposition of a 2.6 μm -thick SiO_x layer using an ICP-CVD tool. A chromium (Cr) hard mask is then prepared through a lift-off process, where Cr is deposited by e-beam sputtering. The SiO_x layer is deeply etched using an ICP-RIE tool, with the Cr mask defining the etch pattern. Finally, the Cr hard mask is removed using a chromium etchant, completing the SiO_x waveguide fabrication.

A spiral waveguide is incorporated into the mask layout to measure the propagation loss of the AlO_x waveguide, as shown in Fig. 5(a). The spiral features a bend radius of 100 μm to minimize bending losses. The cross section of the SiO_x waveguide, after the removal of the Cr mask, is imaged using scanning electron microscope (SEM) and shown in Fig. 5(b). The SiO_x waveguide is designed with dimensions of 3.4 μm wide and 2.6 μm high. Due to the 83 $^\circ$ -angled sidewalls formed during the deep-etching process, the width at the top surface is narrowed to approximately 3.0 μm . Figure 5(c) shows the SEM image of the top view of the AlO_x taper tip. The fabricated width of the taper tip is 61.6 ± 4.6 nm, demonstrating good alignment with the design specifications.

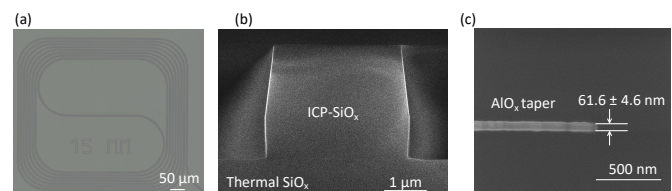


Fig. 5: (a) Optical image of a spiral waveguide. (b) Scanning electron microscope (SEM) image of an ICP- SiO_x waveguide, (c) SEM image of an AlO_x taper tip.

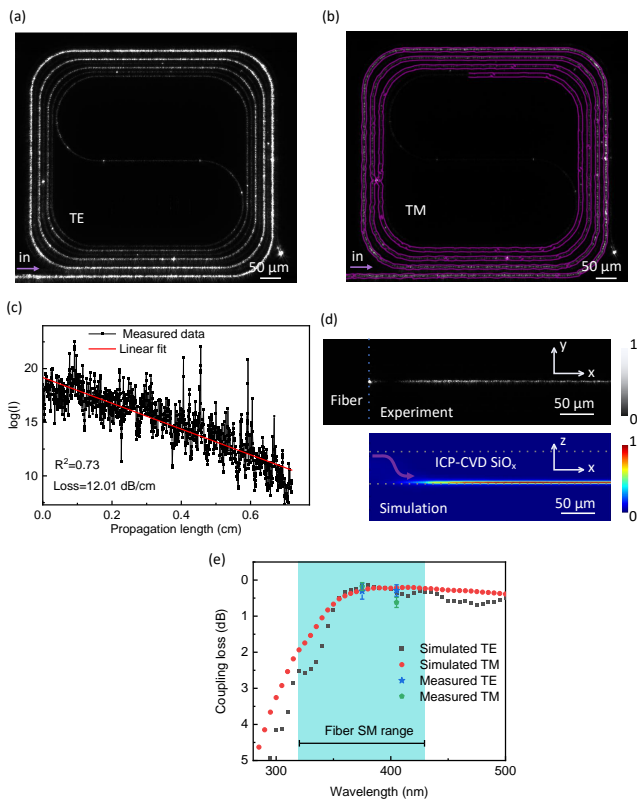


Fig. 6: (a-b) Measured scattered light from a spiral waveguide with TE- and TM-polarized light at $\lambda=375$ nm, respectively. The purple lines in (b) indicate the area where the intensity of scattered light is extracted for propagation loss analysis. (c) Relationship between the log-scale intensity of the scattered light and propagation length for TM-polarized light. (d) Measured (top) scattered light from the edge coupler and simulated (bottom) intensity profiles of light in the edge coupler. (e) Relationship between the coupling loss and wavelength for TE- and TM- polarized light, respectively. Circles and squares represent simulation results. Stars and pentagons indicate measured data.

IV. MEASUREMENT

The propagation loss of the single mode AlO_x waveguide is estimated by analyzing the relationship between the scattered light intensity and the propagation length [5], [17], [18]. Two diode lasers are used for the measurement, one with an emission wavelength of 375 nm (bios375-20fc, elite optoelectronics co. ltd) and the other at 405 nm (LP405-SF10, Thorlabs). Light is coupled from a cleaved single-mode fiber into the AlO_x waveguide, with polarization controlled via a fiber polarization controller. The optical fiber is tightly aligned with the edge of the photonic chip, effectively eliminating light reflection at the interface between the fiber and the edge coupler. The sidewall roughness of the AlO_x waveguide (\sim a few nm) is significantly higher than that of the top surface roughness (\sim 0.3 nm). Consequently, TE-polarized light, which interacts more strongly with the sidewalls, exhibits higher scattering than TM-polarized light, as shown in Figure 6(a) and (b). Due to the high propagation loss of the AlO_x waveguide,

the light cannot propagate through the full 1.5 cm length of the spiral waveguide. Scattered light intensities are extracted along the propagation direction, as indicated in Fig. 6(b), and are plotted in Fig. 6(c). The intensity is averaged over 5 pixels perpendicular to the propagation direction of the light to minimize the impact of imaging aberration. The propagation loss is obtained by performing a linear fit to the measured log-scale intensity, with a value of 12.02 ± 0.38 dB/cm and 12.01 ± 0.20 dB/cm for TE and TM polarization, respectively. ALD AlO_x has been demonstrated to be low loss in the UV range. The relatively high propagation loss is attributed to the sidewall scattering and material absorption, which can be improved by optimizing the etching and deposition recipes. Figure 6(d) presents an optical image of the scattered light from the edge coupler (top) alongside a simulation of light propagation through the edge coupler (bottom). Since both the fiber mode and the SiO_x waveguide mode are relatively large ($\sim \mu\text{m} \times \sim \mu\text{m}$), the light scattering induced by the surface roughness is minimal. However, in the AlO_x taper region, where the light transitions from SiO_x into AlO_x , the mode is confined in a smaller cross-section, increasing its interaction with the AlO_x sidewalls and thereby enhancing scattering. The optical image shows a gradual increase in scattered light intensity along the propagation length, which aligns well with the simulated intensity distribution shown in the bottom image in Fig. 6(d).

In the measurement, an averaged output power are obtained by characterizing two devices. The coupling loss of the edge coupler, α_{EC} , is determined by the input power P_{in} , the output power accounting the photonic chip's insertion loss P_{ipf} , and the propagation loss of the AlO_x waveguide α_{PIC} (in dB) over a given length. The coupling loss is calculated as: $\alpha_{\text{EC}} = -10 \cdot \log(P_{\text{ipf}}/P_{\text{in}}) - \alpha_{\text{PIC}}$. At a working wavelength of 375 nm with TE polarization, the measured input power P_{in} is 3.5 mW and the output power P_{ipf} is 0.61 mW. Based on the propagation loss from Fig. 6(c) and a propagation length of 0.58 cm, the coupling loss is estimated to be 0.31 dB/facet. The standard error is ± 0.22 dB, attributed to the standard error from the linear fitting. Similarly, for TM polarization, the coupling loss is calculated as 0.18 ± 0.11 dB/facet. In addition, to validate the broadband operation of the edge coupler, measurements were also performed at a visible wavelength of 405 nm. The resulting coupling losses were 0.29 ± 0.16 for TE mode and 0.62 ± 0.14 dB/facet for TM modes. These experimental data align well with the simulation results, as shown in Fig. 6(e). The red and black solid curves in Fig.6 (e) represent the coupling loss variation with wavelengths for TE and TM modes, respectively. The low-loss edge coupler exhibits a wide bandwidth that spans the operating wavelength range of single-mode fiber, achieving coupling losses of less than 2.6 dB per facet from 320 to 350 nm and below 1.0 dB per facet from 350 to 430 nm. The coupling loss gradually increases at wavelengths from 430 nm to 500 nm due to mode mismatch loss between the fiber and the SiO_x waveguide. The coupling loss increases at a shorter wavelength below 350 nm due to the increasing mode mismatch at the interface between the SiO_x waveguide and the AlO_x taper. This broadband spectrum covers many critical

wavelengths required for quantum information and advanced life science applications, such as dual-comb gas spectroscopy (344 nm, 388 nm) [19], [20], Yb^+ ion addressing (369.5 nm, 435.5 nm), and Sr^+ ion processing (422 nm, 405 nm) [21]. Table 1 summarizes recent edge coupler designs for the UV and visible spectral regions. To the best of our knowledge, this work achieves the lowest reported coupling loss at a visible wavelength of 405 nm and demonstrates the first edge coupler operating at a UV wavelength of 375 nm.

TABLE I: Comparison of edge coupler designs at UV and visible wavelengths

Material	Wavelength (nm)	Coupling loss (dB/facet)	Year	Reference
SiN	445-640	≤ 4	2021	[22]
	635	4.2	2020	[23]
LN	775	3	2022	[24]
AIO _x	405	8.4	2021	[25]
	405	10.2	2023	[15]
	407	2.85	2024	[16]
	375	0.31	2025	This work
	405	0.62		

V. CONCLUSION

In conclusion, We have proposed an ultra-low-loss edge coupler that operates effectively across the UVC and visible spectrum, demonstrating its viability at wavelengths of 375 nm and 405 nm. The proposed design exhibits robust fabrication tolerance, maintaining a coupling loss below 1 dB for both TE and TM modes, even with taper tip width variations between 10 nm and 90 nm. Additionally, the edge coupler shows high displacement tolerance, with a coupling loss threshold of 3 dB for fiber misalignments up to 1 μ m. The coupling losses of 0.31 dB/facet for TE mode and 0.18 dB/facet for TM mode were achieved experimentally, in good agreement with the simulated values of 0.15 and 0.28 dB/facet, respectively. This edge coupler is expected to serve as a critical building block for UV/Vis photonic integrated platforms, particularly for applications such as PIC-based trapped-ion quantum computing and advanced microscopy, where efficient light coupling, minimal optical losses, and the reduction of spurious light above the chip plane are essential.

ACKNOWLEDGMENTS

C.L. would like to thank Tom Vandekerckhove for valuable discussions regarding the processing of the Cr hard mask.

REFERENCES

- [1] A.-G. Paschke, G. Zarantonello, H. Hahn, T. Lang, C. Manzoni, M. Marangoni, G. Cerullo, U. Morgner, and C. Ospelkaus, "Versatile control of $^9Be^+$ ions using a spectrally tailored uv frequency comb," *Physical Review Letters*, vol. 122, p. 123606, 3 2019.
- [2] W. Eschen, L. Loetgering, V. Schuster, R. Klas, A. Kirsche, L. Berthold, M. Steinert, T. Pertsch, H. Gross, M. Krause, J. Limpert, and J. Rothhardt, "Material-specific high-resolution table-top extreme ultraviolet microscopy," *Light: Science & Applications*, vol. 11, p. 117, 4 2022.
- [3] S. A. Oladepo, K. Xiong, Z. Hong, S. A. Asher, J. Handen, and I. K. Lednev, "Uv resonance raman investigations of peptide and protein structure and dynamics," *Chemical Reviews*, vol. 112, pp. 2604–2628, 5 2012.
- [4] W. Hendriks, M. Dijkstra, S. Mardani, I. Hegeman, and S. García-Blanco, "Low-loss photonic integrated circuits for uv applications," in *Integrated Optics: Devices, Materials, and Technologies XXVII*, S. M. García-Blanco and P. Cheben, Eds. SPIE, 3 2023, p. 2.
- [5] C. Lin, D. Schaubroeck, R. Baets, N. Boon, and N. L. Thomas, "Uv photonic-integrated-circuits-based structured illumination microscopy with a field of view larger than $100 \mu\{m\}^{\{2\}}$," *IEEE Journal of Selected Topics in Quantum Electronics*, vol. 29, pp. 1–9, 7 2023.
- [6] G. N. West, W. Loh, D. Kharas, C. Sorace-Agaskar, K. K. Mehta, J. Sage, J. Chiaverini, and R. J. Ram, "Low-loss integrated photonics for the blue and ultraviolet regime," *APL Photonics*, vol. 4, pp. 26 101–26 107, 2019.
- [7] B. Pan, J. Bourderionnet, V. Billault, G. Dande, M. Dahlem, J. H. Song, S. Dwivedi, D. C. Altamirano, C. Cummins, S. S. Saseendran, P. Helin, J. Ramirez, D. Néel, E. Soltanian, J. Zhang, and G. Roelkens, "Ii-v-on-si₃n₄ widely tunable narrow-linewidth laser based on micro-transfer printing," *Photonics Research*, vol. 12, p. 2508, 11 2024.
- [8] I. L. Lufungula, A. Shams-Ansari, D. Renaud, C. O. de Beeck, S. Cuyvers, S. Poelman, M. Billet, G. Roelkens, M. Lončar, and B. Kuyken, "Integrated resonant electro-optic comb enabled by platform-agnostic laser integration," *Laser & Photonics Reviews*, vol. 18, 10 2024.
- [9] T. Vanackere, T. Vandekerckhove, L. Bogaert, M. Billet, S. Poelman, S. Cuyvers, J. V. Kerrebrouck, A. Moerman, O. Caytan, N. Singh, S. Lemey, G. Torfs, P. Ossieur, G. Roelkens, S. Clemmen, and B. Kuyken, "Heterogeneous integration of a high-speed lithium niobate modulator on silicon nitride using micro-transfer printing," *APL Photonics*, vol. 8, 8 2023.
- [10] S. Bernal, M. Dumont, E. Berikaa, C. St-Arnauld, Y. Hu, R. G. Castrejon, W. Li, Z. Wei, B. Krueger, F. Pittalà, J. Bowers, and D. V. Plant, "12.1 terabit/second data center interconnects using o-band coherent transmission with qd-mll frequency combs," *Nature Communications*, vol. 15, p. 7741, 9 2024.
- [11] C. Lin, J. Peñaranda, J. Dendooven, C. Detavernier, D. Schaubroeck, N. Boon, R. Baets, and N. L. Thomas, "Uv photonic integrated circuits for far-field structured illumination autofluorescence microscopy," *Nature Communications*, vol. 13, 2022.
- [12] C. Lin, Y. Guo, and N. L. Thomas, "Demonstration of a photonic integrated circuit for quantitative phase imaging," *Photonics Research*, vol. 13, p. 1, 1 2025.
- [13] J. Kwon, W. J. Setzer, M. Gehl, N. Karl, J. V. D. Wall, R. Law, M. G. Blain, D. Stick, and H. J. McGuinness, "Multi-site integrated optical addressing of trapped ions," *Nature Communications*, vol. 15, p. 3709, 5 2024.
- [14] C. D. Bruzewicz, J. Chiaverini, R. McConnell, and J. M. Sage, "Trapped-ion quantum computing: Progress and challenges," *Applied Physics Reviews*, vol. 6, 2019.
- [15] C. Franken, W. Hendriks, M. Dijkstra, A. do Nascimento, L. Winkler, A. van Rees, S. Mardani, R. Dekker, J. van Kerckhof, P. van der Slot, S. García-Blanco, and K.-J. Boller, "First near-uv hybrid integrated laser in the al₂o₃ platform," in *Integrated Optics: Devices, Materials, and Technologies XXVII*, S. M. García-Blanco and P. Cheben, Eds. SPIE, 4 2023, p. 22.
- [16] Y. Du, X. Ji, W. Xie, Y. He, Y. Zhang, M. Tian, and Y. Su, "High-efficiency fiber-chip edge coupler for near-ultraviolet integrated photonics," *Advanced Materials Technologies*, vol. 9, 8 2024.
- [17] C. Su, C. A. J. Concha, C. Lin, N. Quack, C. Galland, and N. L. Thomas, "Low-loss and high-index contrast ultraviolet-c free-standing waveguides made of thermal silicon oxide," *Optics Letters*, vol. 49, p. 3785, 7 2024.
- [18] S. R. Sørensen, E. Z. Ulsig, F. E. Philip, F. R. B. Sørensen, M. L. Madsen, A. B. Gardner, P. Tønning, S. T. Thomsen, K. B. Gravesen, E. J. Stanton, and N. Volet, "Open-source toolbox for photographic characterization of optical propagation," *Optics Letters*, vol. 49, p. 4098, 8 2024.
- [19] B. Xu, Z. Chen, T. W. Hänsch, and N. Picqué, "Near-ultraviolet photon-counting dual-comb spectroscopy," *Nature*, vol. 627, pp. 289–294, 3 2024.
- [20] L. Fürst, A. Kirchner, A. Eber, F. Siegrist, R. di Vora, and B. Bernhardt, "Broadband near-ultraviolet dual comb spectroscopy," *Optica*, vol. 11, p. 471, 4 2024.
- [21] R. J. Niffenegger, J. Stuart, C. Sorace-Agaskar, D. Kharas, S. Bramhavar, C. D. Bruzewicz, W. Loh, R. T. Maxson, R. McConnell, D. Reens, G. N. West, J. M. Sage, and J. Chiaverini, "Integrated multi-wavelength control of an ion qubit," *Nature*, vol. 586, pp. 538–542, 2020.
- [22] Y. Lin, J. C. C. Mak, H. Chen, X. Mu, A. Stalmashonak, Y. Jung, X. Luo, P. G.-Q. Lo, W. D. Sacher, and J. K. S. Poon, "Low-loss broadband bi-

- layer edge couplers for visible light,” *Optics Express*, vol. 29, p. 34565, 10 2021.
- [23] N. C. Lin, S. Hassan, X. Zhao, A. Veeraraghavan, and J. T. Robinson, “High coupling efficiency, passive alignment setup for visible-range fiber-to-waveguide edge coupling,” *Journal of Nanophotonics*, vol. 14, 12 2020.
- [24] X. Liu, S. Gao, C. Zhang, Y. Pan, R. Ma, X. Zhang, L. Liu, Z. Xie, S. Zhu, S. Yu, and X. Cai, “Ultra-broadband and low-loss edge coupler for highly efficient second harmonic generation in thin-film lithium niobate,” *Advanced Photonics Nexus*, vol. 1, 6 2022.
- [25] R. Morgan, D. Kharas, J. Knecht, P. Juodawlkis, K. Cahoy, and C. Sorace-Agaskar, “Waveguide-integrated blue light detector,” in *2021 IEEE Photonics Conference (IPC)*. IEEE, 10 2021, pp. 1–2.